ARTICLE   OPEN

Check for updates

Sea surface temperature warming to inhibit mitigation of tropical cyclone destructiveness over East Asia in El Niño

Doo-Sun R. Park[1] ✉, Eunkyo Seo [2,3], Minkyu Lee [4], Dong-Hyun Cha [5] ✉, Dasol Kim[6], Chang-Hoi Ho[7], Myong-In Lee[5], Hyeong-Seog Kim [8] and Seung-Ki Min [4,9]

Given their conditions to reside in and intensify longer over warm oceans, tropical cyclones (TCs) in the western North Pacific (WNP) present a stronger lifetime maximum intensity during El Niño than during La Niña. By using observational data, we found that the anomalously cool sea surface temperature (SST)s in the basin act as effective barriers against intense TCs approaching East Asia during El Niño, weakening their destructiveness at landfall. Based on our high-resolution pseudo-global-warming simulations, the basin-wide 2K SST warming within the WNP basin can, however, shatter this cool SST barrier, exposing East Asia to more destructive TCs during El Niño, compared to those during La Niña. Considering that the 2K warmer WNP will likely occur in the mid-21st century under a high emission scenario and in the late 21st century under a moderate emission scenario, our findings support that more aggressive efforts of global warming mitigation are needed.

INTRODUCTION

Tropical cyclones (TCs) are primarily active in the western North Pacific (WNP). On an annual average, ~25 TCs form in the basin, accounting for 25% of the total global TCs[1,2], half of which strike East Asia, including Korea, Japan, and China. The damages caused consequently amount to an annual average of USD 0.5 billion per TC[2]. The financial losses incurred by a TC are determined based on various factors, particularly, the TC intensity at landfall (landfall intensity);[3,4] stronger landfall intensities are generally associated with greater damage, and thus unprecedented landfall intensities imply catastrophic damage. The Typhoon Maemi, which struck the Republic of Korea in 2003, is one such TC. With a record-breaking landfall intensity of ~54 m s^{-1} [5,6], the TC incurred property losses of USD ~ 5 billion—the largest ever reported. In light of these events, the Korean government was pressured to enhance the windproof design to protect infrastructure against wind gusts. Such events highlight the importance of understanding inter-annual TC variability, especially in terms of landfall intensity.

The El Niño Southern Oscillation (ENSO)—the spatiotemporal variability of sea surface temperature (SST) in the tropical Pacific[7]—is the most dominant driver of TC intensity over the WNP on interannual time scales[8–11]. ENSO significantly shifts the location of TC genesis, inducing interannual variability of TC intensity; during El Niño, TCs tend to form in the southeastern part of the basin, whereas during La Niña, they tend to form in the northwestern part. Since the TCs in the WNP translate north-westward in the tropics, more TCs generated in the southeastern WNP indicates that, considering the northwest-continent and southeast-ocean geographical distribution, TCs can stay longer over the warm oceans before they landfall[8]. Consequently, the TC intensity increases considerably during El Niño compared to that during La Niña.

However, the robust relationship between ENSO and TC intensity holds only for lifetime maximum intensity (LMI), lifetime average intensity, or lifetime cumulative indices such as accumulated cyclone energy and power dissipation index[8–10]. Zheng et al[12]. inspired us that ENSO may not be a controlling factor for landfall intensity. They found a loosening factor for the positive correlation between ENSO and LMI. The study indicated that the upper ocean heat content over the WNP reduces during El Niño than that during La Niña, which strengthens the cooling effect by TC-induced upwelling. The upwelling draws colder water from below, creating unfavorable conditions for TC intensification; consequently, the effect of a longer lifetime for TC intensification diminishes. This Gaia-like mechanism works consistently for different El Niño types[12], that is, the warm pool and cold tongue El Niños[13]. This mechanism can further affect TC intensification if we focus on landfall rather than on LMI; however, few studies have addressed this topic.

In addition to the ocean heat content[14–17], the response of basin-wide SST in the WNP to ENSO is thought to be an important influential factor controlling the TC development and intensification. The basin-wide SST in the WNP generally becomes cooler than normal in El Niño, while it becomes warmer in La Niña[18,19]. The SST patterns roughly correspond to the potential intensity (PI), which represents the theoretical maximum wind speed at which a TC can reach a region[20–22]. According to Xu and Wang[23], the maximum potential intensification rate of TCs is primarily associated with SST, and the most intensifying TCs have been reported for regions where the SSTs are higher than 28℃. These facts suggest that even without considering the ocean heat content, SST conditions can exert a damping effect on TC intensification, thus weakening the landfall intensity during El Niño.

---

[1]Department of Earth Science Education, Kyungpook National University, Daegu, Buk-gu 41566, South Korea. [2]Department of Environmental Atmospheric Sciences, Pukyong National University, Namgu, Busan 48513, South Korea. [3]Center for Ocean-Land-Atmosphere Studies, George Mason University, Fairfax, VA 22030, USA. [4]Division of Environmental Science and Engineering, Pohang University of Science and Technology, Pohang, Gyeongbuk 37673, South Korea. [5]Department of Civil, Urban, Earth, and Environmental Engineering, Ulsan National Institute of Science and Technology, Ulju-gun, Ulsan 44919, South Korea. [6]Department of Geography, University of Florida, Gainesville, FL 32611, USA. [7]Department of Climate and Energy Systems Engineering, Ewha Womans University, Seodaemun-gu, Seoul 03760, South Korea. [8]Ocean Science and Technology School, Korea Maritime and Ocean University, Yeongdo-gu, Busan 49112, South Korea. [9]Institute for Convergence Research and Education in Advanced Technology, Yonsei University, Seoul, Seodaemun-gu 03722, South Korea. ✉email: dsrpark@knu.ac.kr; dhcha@unist.ac.kr

In this study, we identified the effects of cool SST barriers on landfall intensity during El Niño events and investigated its changes in a warmer climate. In particular, only the TCs striking mid-latitude East Asia, that is, land areas above 30°N, including East China, Korea, and Japan, were considered, because TCs migrating up to mid-latitude East Asia generally stay over the ocean longer than those that do not, thus maximizing the SST effects. In addition, if only TCs landfalling north of 30°N are considered, the track change effects on TC intensity according to ENSO phases can be minimized. In general, TCs tend to recurve to the mid-latitudes during El Niño and move straight to the subtropics during La Niña[24,25]. This causes more TCs to experience cooler mid-latitude oceans on their pathways after LMI during El Niño, contributing to the overall variations in landfall intensity, even without any change in basin-wide SSTs, if we consider both TC-prone subtropical and mid-latitude areas of East Asia. The response of track changes to ENSO becomes further complicated when considering sub-seasons (e.g., early and late seasons) or different types of ENSO[26–30]. However, even when assuming possible track differences, their effects on landfall intensity above 30°N are expected to be minor. This is because the track difference is mainly longitudinal in TCs heading to the mid-latitude[31,32] while the zonal SST variations are much smaller than the meridional variations[21].

RESULTS

Mitigating effect of cool WNP SST in landfall intensity over East Asia during El Niño

Our observational analyses on landfall intensities indicated no significant differences between El Niño and La Niña (Table 1 and Supplementary Table 1). The mean genesis location shifts significantly southeast in El Niño years, so that LMI before landfall is 10.42 m s^{-1} greater in El Niño than in La Niña years due to the longer lifetime, which is significant at the 90% confidence level. This is consistent with the well-known responses of TC activity to ENSO in the WNP[8–10,28]. The average location of the LMI shows the same response to ENSO as that of its genesis location—it moves southeastward during El Niño and northwestward during La Niña. This is also consistent with a previous study[25], although we only considered TCs entering the mid-latitudes of East Asia. The southeastward retreat of the LMI during El Niño indicates early decay of a TC, which means that the TC intensity decreases for a substantial time prior to landfall. Consequently, the landfall intensity during El Niño is comparable to that during La Niña, although the LMI during El Niño is stronger than that during La Niña. Hence, it is important to understand the factors that determine the response of LMI locations to ENSO. Meanwhile, when considering only TCs striking south of 30°N, we could not find the significant difference in LMI and its location as well as landfall intensity (Supplementary Table 2). As discussed in the introduction, this is because TCs striking countries in the subtropics have relatively little time to develop over the warm ocean; they have about 20 hours shorter lifetime from genesis to LMI than TCs striking the mid-latitudes. This result further supports our focus on TCs landfalling north of 30°N.

Our results indicate that the SST acts as a key factor with regards to variations in the LMI locations associated with ENSO (Fig. 1). The SST becomes cooler during El Niño than during La Niña over the entire WNP basin. The relative unfavourability of cooler SST to TC intensification forces the TC to reach LMI farther from land during El Niño. Specifically, the 28−29°C band is an important baseline upon which the average LMI location for both El Niño and La Niña falls. Our results are consistent with those of a previous study highlighting 28°C as an empirical baseline of intensification[23].

Figure 2 further emphasizes that SST is a much more critical factor than other well-known factor, vertical wind shear (VWS)[23]. The linear relationship is significant (r = 0.47) between the SST and TC intensification rate (Fig. 2a), which was significant at the 95% confidence level, while a relatively low correlation coefficient (r = 0.16) is shown between VWS and TC intensification rate (Fig. 2b). In order to emphasize the robust relationship between SST and TC intensification rate compared to VWS, VWS and SST are additionally plotted in colors in Figs. 2a and 2b, respectively. The colors of the dots in Fig. 2a, representing the VWS, are not well separated into red (high VWS) and blue (low VWS) above and below the zero-intensification rate, respectively, whereas in Fig. 2b the red (high SST) and blue (low SST) colors are clearly separated above and below the zero-intensification rate, respectively. In other words, VWS is not a critical factor in determining the intensification rate, while SST is critical in determining the intensification rate. Meanwhile, 700-hPa relative humidity and 850-hPa relative vorticity, known as other factors, are not important for the TC intensification rate, as their correlation coefficients with the TC intensification rate are 0.2 and −0.01, respectively.

Disappearance of cool SST barrier against catastrophic TC landfall over East Asia during El Niño under the pseudo-global warming

Our results suggest that cooler basin-wide SSTs during El Niño can act as successful barriers against intense TCs approaching the mid-latitudes in East Asia. However, this barrier might only work under present climatic conditions given that global warming can lead to an increase in the SST in the WNP. The basin-wide SST warming can relocate the 28°C SST baseline poleward such that the cool SST barrier is no longer valid, particularly during El Niño. To support this hypothesis, pseudo-global-warming experiments with a very high horizontal resolution (3 km) and large domain were performed for three representative cases of each ENSO phase (see Methods for details). Given the limited computing resources, we selected the following representative cases with general, well-known characteristics for each ENSO phase (Supplementary Table 3): farther and

Table 1. Average locations (in latitude and longitude) and average maximum sustained wind speed (MSWS; m s^{-1}) at genesis, lifetime maximum intensity (LMI), tropical cyclone (TC) landfall, and 30°N during El Niño and La Niña, and their differences.

	El Niño			La Niña			El Niño minus La Niña		
	Longitude	Latitude	MSWS	Longitude	Latitude	MSWS	Longitude	Latitude	MSWS
Genesis of landfall TCs	144.26	14.04	–	133.90	20.71	–	+10.35**	−6.67**	–
LMI of landfall TCs	135.14	21.83	56.54	130.32	27.33	46.12	+4.82*	−5.51**	+10.42*
Landfall	131.31	33.36	29.88	129.72	33.30	31.54	+1.59	+0.06	−1.66
30°N	129.59	30.09	36.57	128.90	30.06	35.21	+0.69	+0.02	+1.36

Single (*) and double (**) asterisks indicate that the difference is significant at the 90% and 99% confidence levels, respectively, based on the Student's t-test. MSWS at genesis is omitted since it is almost always 17 m s^{-1} per the definition of genesis in the present study.
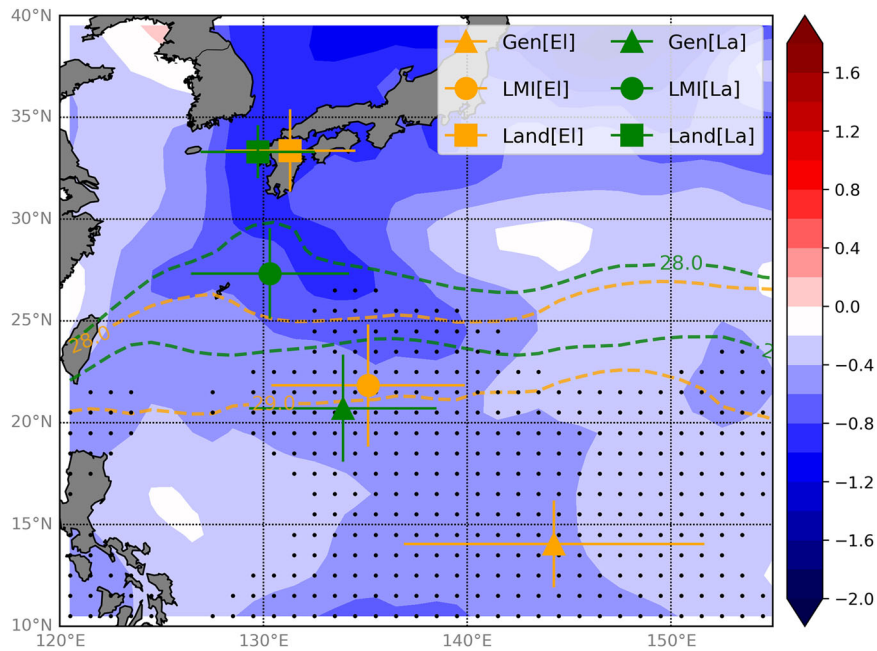
Fig. 1 Differences in sea surface temperatures (SST) between El Niño and La Niña years during tropical cyclone (TC) season, that is, from June to October (shading and contour; unit of °C). Gen, LMI, and Land (triangle, circle, and rectangular, respectively) indicate mean locations of genesis, lifetime maximum intensity (LMI), and landfall, respectively. El and La within square brackets represent El Niño and La Niña, respectively. Black dots indicate that the difference is significant at the 99% confidence level, based on the Student's t-test.
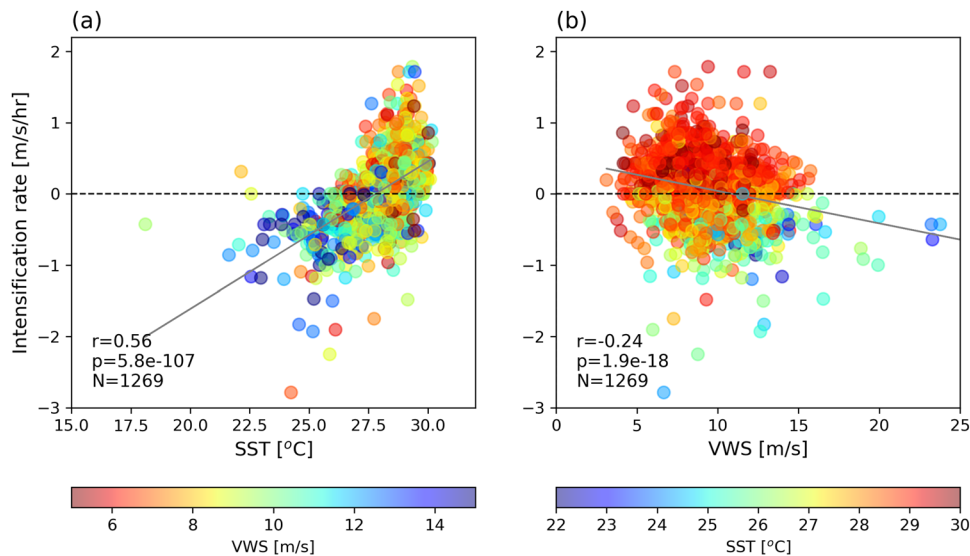
Fig. 2 Scatter plots. a Sea surface temperature (SST) and **b** vertical wind shear (VWS) versus intensification rate. Solid lines indicate the linear fit slopes of the scatters; dashed lines indicate zero intensification rate. Colors in (**a**) and (**b**) represent VWS and SST, respectively. In the lower left of each panel, r, p val, and N indicate the Pearson correlation coefficient, its p value, and the number of samples, respectively.

closer TC genesis and LMI locations from the East Asian continent during El Niño and La Niña, respectively.

Despite some limitations, the model captures well the main features of intensity variation with latitude. The lower maximum sustained wind speed (MSWS) values in the models than in the observations are particularly evident for El Niño cases (Fig. 3), although the model experiments yielded comparable observational TC tracks (Supplementary Figure 1). This suggests that the model does not accurately reproduce catastrophically intense TCs during El Niño, even at a high resolution of 3 km. Nevertheless, in both the observation and the control run, the LMI consistently appeared at 20−25°N during El Niño and above 30°N during La

Niña. Similar to the observations, the LMI location for La Niña in the model was closer to mid-latitude East Asia than during El Niño. In addition, the MSWS at 30°N during El Niño (31.16 m s^{-1}) and La Niña (31.24 m s^{-1}) are comparable, which is consistent with observations showing comparable intensities between El Niño (36.57 m s^{-1}) and La Niña (35.21 m s^{-1}) (see Tables 1 and 2). In the model, the MSWS at 30°N has been regarded as the landfall intensity because most mid-latitude coastlines are located near 30°N. We did not investigate landfall intensity per se in the model because the simulated TC tracks were not exactly the same between the present and 2K warming climate (Supplementary Figure 1). Therefore, the landfall intensities cannot be directly
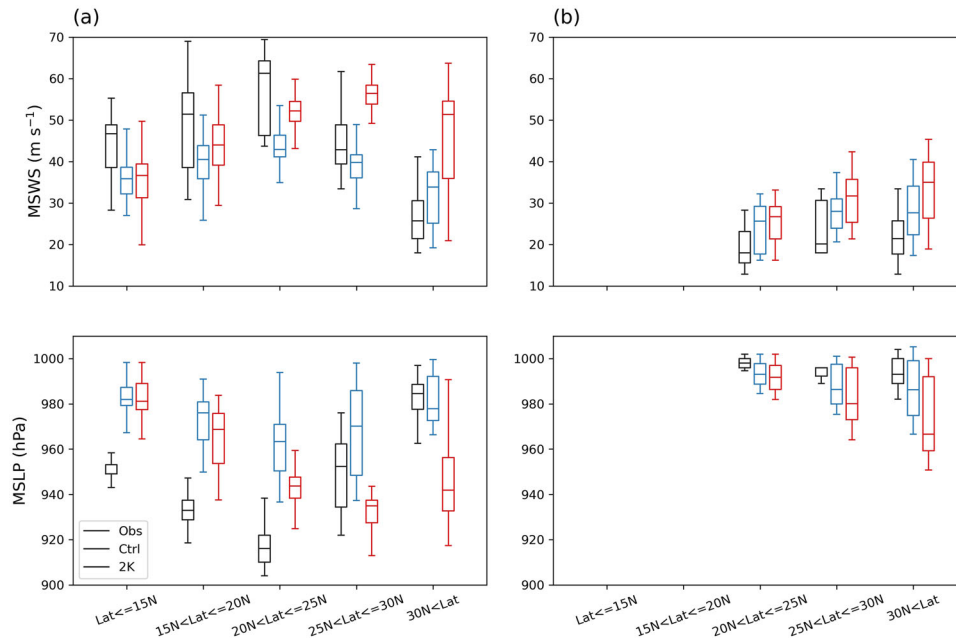
(a)

(b)

Fig. 3 **Box plots of maximum sustained wind speed (MSWS, upper panels) and minimum sea level pressure (MSLP, lower panels) at each latitude band for observation (Obs), control (Ctrl), and 2K-warming (2K) experiments.** El Niño and La Niña cases are shown in (**a**) and (**b**), respectively. The upper, middle, and lower bars in the box indicate the 75% (Q3), median, and 25% (Q1) values. The upper and lower whiskers indicate Q3 + 1.5×(Q3 − Q1) and Q1 − 1.5×(Q3 − Q1), respectively. MSWS was collected at each 6-hour position in each latitude interval.

Table 2.	Averages of maximum sustained wind speed (m s^{-1}) at 30°N during El Niño and La Niña for control (Ctrl) and 2K-warming experiments (2K), and the differences between El Niño and La Niña for each experiment, and 2K and Ctrl for each ENSO phase.		
	El Niño	La Niña	Diff. between El Niño and La Niña
Ctrl	31.16	31.24	−0.08
2K	41.95	30.88	+11.07**
Diff. between 2K and Ctrl	+10.79**	−0.36	

Double asterisks (**) indicate that the difference is significant at the 99% confidence level, based on the Mann–Whitney U test.

compared. The observational results are not sensitive to the use of two different terms, that is, landfall intensity and MSWS at 30 °N (Table 1 and Supplementary Table 1); both landfall intensity and MSWS at 30°N show little difference between El Niño and La Niña.

According to the model experiments, basin-wide 2K uniform SST warming can lead to a stronger landfall intensity during El Niño than during La Niña (Fig. 3 and Table 2). Under present climatic conditions, the TC may approach its LMI location at 20−25°N during El Niño but above 30°N during La Niña. In the 2K warming climate, the TC reaches its LMI location at 25−30°N in El Niño, and further the MSWS decays slowly until the TC reaches 30°N. In contrast, since the upper limit of the LMI latitude prior to landfall is 30°N, the LMI location cannot migrate further poleward in La Niña. For 2K warming, the mean MSWS at 30°N increases by ~10.79 m s^{-1} in El Niño (41.95 m s^{-1}), whereas in La Niña it barely changes from 31.24 m s^{-1}.

DISCUSSION

Our results show that SST is a good and simple indicator of TC intensification, as we already knew. PI may be a more accurate indicator of TC intensification because it includes not only surface

conditions but also tropospheric conditions. We found that PI is significantly correlated with TC intensification rate (r = 0.6), as is SST. However, the consistency of high correlations of SST and PI with the intensification rate implies that SST is rather a better indicator of TC intensification, despite the lack of information on tropospheric state, because it is a much simpler indicator than PI. PI requires 3D variables such as temperature and humidity. This can also be supported by previous studies, which showed that PI patterns almost correspond to SST as mentioned in the introduction[20–22].

According to our result, the LMI and its location are not a critical factor for landfall intensity, but rather the SST. At first sight, our result seems to contradict a previous study[33] which argued that the LMI and its location are important in determining the landfall intensity; both a large LMI and a small distance between the LMI and the landfall location lead to catastrophic TC landfalls. However, a closer look at the results leads to the same conclusion. The discrepancy may be due to two reasons. First, we used only the mid-latitude TCs associated with each ENSO phase, whereas the previous study[33] used all TCs. Second, the previous study[33] identified a possible double requirement of TCs with LMI greater than 50 m s^{-1} and proximity to land for the most damaging cases with landfall intensity greater than 50 m s^{-1}. In contrast, we have considered all intensity categories, both in terms of LMI and landfall intensity. However, under our 2K warming simulation, both the landward extension of the LMI, i.e. about 5 degrees poleward, and the increased LMI per se with an intensity greater than 50 m s^{-1}, especially during El Niño, lead to the catastrophic landfall intensity. This is a similar sampling as in the previous study[33]. In this respect, our results are in agreement with the previous study[33].

In our model experiment, MSWS was simulated much weaker than observed particularly during El Niño. This could be due to the different environmental conditions between model and observation. In particular, we focused on the thermodynamic conditions. As a representative, for the case of typhoon TINA, the PI calculated in the model over the WNP basin was only about 10% lower than that of the observation. This means that the different thermodynamic

background was not a critical factor leading to significantly weaker MSWS in the model than in the observation, but rather the other inherent limitations such as resolution, physics, etc. could be.

In conclusion, under the present climate, the cool SST barrier inhibits destructive TCs from approaching mid-latitude East Asia during El Niño compared with that during La Niña. Despite several limitations, our study provides the evidence that future warmings may allow catastrophic TC landfall over highly populated East Asia during El Niño events by eliminating the SST barrier. This highlights the importance of responding properly to future risks of intense TC exposures that accompany El Niño.

The recent international movement toward global carbon neutrality can effectively delay the timing of the TC destruction of the cool SST barrier during El Niño. To assess the relevance of our hypothetical warming for the future emission scenarios, i.e., the Shared Socioeconomic Pathway (SSP) scenario, we have checked the timing of the 2K SST warming with respect to the current period (1979−2014) in the WNP as well as in the global ocean using 29 climate models. Results show that the ensemble mean SST warming in the WNP is estimated to exceed 2K in 2060 under the SSP5-8.5 scenario and in 2096 under the SSP2-4.5 scenario. This indicates that our experiment based on regional 2K warming corresponds to the future conditions in the mid-21st century under high emission scenario (SSP5-8.5) or in the late 21th century under moderate emission scenario (SSP2-4.5). Note that this emergence of regional 2K warming is slightly faster than that of global mean SST, which occurs in 2067 under the SSP5-8.5 scenario but not within this century under the SSP2-4.5 scenario. This timing result supports the necessity of more aggressive efforts of global warming mitigation to minimize the possible impacts of stronger TCs on East Asia.

METHODS

Data and methodology

This study used the best track datasets from the Joint Typhoon Warning Center (JTWC) released by the Naval Meteorology and Oceanography Command. To reduce data uncertainty, we also used the best track dataset from the Regional Specialized Meteorological Center (RSMC) as a supplement. Briefly, 6-hourly datasets for the center locations of TCs, sea level pressure, and MSWS were provided by above agencies. To accurately capture landfall in mid-latitude East Asia and its intensity at that time, 6-hourly TC data were linearly interpolated to 1-hourly data. This is because a 6-hour interval is too long to detect a precise landfall over the relatively narrow land areas in the mid-latitudes, such as the Korean peninsula and the Japanese islands[34]. Note that the interpolated data have only been used in Table 1 and the Supplementary Tables 1 and 2. In Fig. 3 and Table 2, 6-hourly data were utilized to preserve the originality of the data as much as possible. A location was defined as TC's genesis when the TC firstly reached its MSWS in excess of tropical storm intensity, that is, $17\,m\,s^{-1}$. If TCs reached $17\,m\,s^{-1}$ at least once, all TC intensity categories, including typhoons (MSWS $\geq 33\,m\,s^{-1}$), tropical storms ($33\,m\,s^{-1} >$ MSWS $\geq 17\,m\,s^{-1}$), and tropical depressions ($17\,m\,s^{-1} >$ MSWS $\geq 12\,m\,s^{-1}$), were included in the calculation. Only those TCs whose genesis was located within the WNP (120–180°E and 0–40 °N) generated during the TC season from June to October were used in the calculation. Landfall was defined as the timing when a TC first crossed the coastlines of Korea, Japan, and east China above 30°N. MSWS at landfall was defined as landfall intensity. If a TC migrated westward across the 122°E line prior to reaching 30°N, the TC was excluded from the calculation; this is because such TC types make a landfall in mainland China before reaching 30°N.

Large-scale background states such as the SST and VWS surrounding the TCs were examined using the daily Optimum Interpolation SST version 2 (OISSTv2)[35] and ERA5 reanalysis data from the European Centre for Medium-Range Weather Forecasts (ECMWF)[36]. Both datasets have spatial resolutions of ~25 km and daily temporal resolution. The VWS was calculated from the wind difference between 850 hPa and 200 hPa. To examine the relation between TC characteristics and environmental conditions (Fig. 2), all variables, such as SST and VWS, were averaged daily over the area between 200 km and 800 km from the TC center[37], and compared with average TC intensification rate at that day. This is because the OISST data are daily data. A total of 1246 samples were used for these calculations.

TC's sensitivity to ENSO is characterized by standardized SST anomalies over the Niño3.4 region (5°N–5°S, 170–120°W) during the TC season (June to October). The El Niño and La Niña years were defined when the Niño3.4 index became larger than 0.95 and lower than −0.95, respectively[11,38]. Over the analysis periods (1979−2018), we identified the same number of years for each ENSO phase: five El Niño years (1982, 1987, 1997, 2002, and 2015) and five La Niña years (1988, 1998, 1999, 2007, and 2010). Note that even if we use 1 as the threshold, the main result does not change significantly (not shown). As such, using the annual mean values of TC characteristics (e.g., LMI and landfall intensity) would have yielded very few number of samples. Hence, we considered each TC's characteristics for each ENSO phase during calculation and obtained 24 and 19 TC cases for El Niño and La Niña, respectively. In case of the RSMC, 25 and 20 cases of El Niño and La Niña events were obtained, respectively. This approach allowed us to acquire a greater number of samples to test statistical significance. All significance tests were performed using the Student's t-test, except for Table 2, where the Mann–Whitney U test was additionally used as the sample number for each case in there was < 12—too small to hypothesize normal distributions.

For the basin average SST over the WNP (100°E–180°N and 0–40°N), 29 climate model simulations under the SSP scenarios (i.e. SSP2-4.5 and SSP5-8.5) in the Coupled Model Intercomparison Project Phase 6 (CMIP6) were utilized. The models used in this study are listed in Supplementary Table 4.

Model description and experiments

The Weather Research and Forecasting (WRF) model (version 4.1.2) was used to identify warming effects[39]. The ERA5 reanalysis data, which covers Earth with a 0.25° × 0.25° horizontal resolution, were used as initial and boundary conditions[36]. Prescribed daily SST was obtained from OISSTv2[35]. The horizontal grid spacing of the WRF was 3 km with a single domain that covered most of the WNP (approximately 0–50°N, 100–175°E), with 2481 × 1921 grid points in the zonal and meridional directions. The model had 50 vertical levels from the surface to the top of the atmosphere at 50 hPa. A multi-physics ensemble approach was applied to reduce the uncertainties in the WRF simulations. Four ensemble members were constructed for each TC case using two cumulus parameterization schemes (multi-scale Kain–Fritsch and KIM Simplified Arakawa–Schubert) and two microphysics parameterization schemes (WRF single-moment 6-class and WRF double-moment 6-class) (Supplementary Table 3)[40–43]. The WRF model uses the following parameterization schemes: the Yonsei University (YSU) planetary boundary layer scheme[44,45], Rapid Radiative Transfer Model (RRTM) long-wave, and Dudhia short-wave radiation scheme[46,47].

Six TCs were selected for the case study (three each of El Niño and La Niña). The simulation periods for each TC case are listed in Supplementary Table 3. The control (Ctrl) experiments used the SST from TC simulation data, and 2K experiments used a 2K warmer SST than did the Ctrl experiment. Other variables were applied equally in both the Ctrl and 2K experiments. For each El Niño and La Niña, the warming effect was examined by comparing

the results of two experiments. According to the previous studies, the pseudo-global warming experiments require at least one day of spin-up[48,49], so the first 24 hours of data from the initial state were excluded from the analysis for Fig. 3.

REFERENCES

1. Webster, P. J., Holland, G. J., Curry, J. A. & Chang, H.-R. Changes in tropical cyclone number, duration, and intensity in a warming environment. *Science* **309**, 1844–1846 (2005).
2. Basconcillo, J. & Moon, I.-J. Increasing activity of tropical cyclones in East Asia during the mature boreal autumn linked to long-term climate variability. *npj Clim. Atmos. Sci.* **5**, 4 (2022).
3. Park, D.-S. R., Ho, C.-H., Nam, C. C. & Kim, H.-S. Evidence of reduced vulnerability to tropical cyclones in the Republic of Korea. *Environ. Res. Lett.* **10**, 054003 (2015).
4. Bakkensen, L. A., Park, D.-S. R. & Sarkar, R. S. R. Climate costs of tropical cyclone losses also depend on rain. *Environ. Res. Lett.* **13**, 074034 (2018).
5. Kim, J.-M., Son, K., Yum, S.-G. & Ahn, S. Typhoon Vulnerability Analysis in South Korea Utilizing Damage Record of Typhoon Maemi. *Adv. Civ. Eng.* **2020**, 8885916 (2020).
6. Kim, J.-M., Kim, T., Son, K., Yum, S.-G. & Ahn, S. Measuring Vulnerability of Typhoon in Residential Facilities: Focusing on Typhoon Maemi in South Korea. *Sustainability* **11**, 2768 (2019).
7. Trenberth, K. E. The Definition of El Niño. *Bull. Am. Meteorol. Soc.* **78**, 2771–2778 (1997).
8. Camargo, S. J. & Sobel, A. H. Western North Pacific tropical cyclone intensity and ENSO. *J. Clim.* **18**, 2996–3006 (2005).
9. Chen, T.-C., Wang, S.-Y. & Yen, M.-C. Interannual variation of the tropical cyclone activity over the western North Pacific. *J. Clim.* **19**, 5709–5720 (2006).
10. Zhao, H., Wu, L. & Zhou, W. Interannual changes of tropical cyclone intensity in the western North. *Pac. J. Meteorol. Soc. Jpn.* **89**, 243–253 (2011).
11. Seo, E. et al. Inter-annual variation of tropical cyclones simulated by GEOS-5 AGCM with modified convection scheme. *Int. J. Climatol.* **39**, 4041–4057 (2019).
12. Zheng, Z.-W., Lin, I.-I., Wang, B., Huang, H.-C. & Chen, C.-H. A long neglected damper in the El Nino-typhoon relationship: a 'Gaia-like' process. *Sci. Rep.* **5**, 11103 (2015).
13. Kug, J.-S., Jin, F.-F. & An, S.-I. Two types of El Niño events: Cold tongue El Niño and warm pool El Niño. *J. Clim.* **22**, 1499–1515 (2009).
14. Lin, I.-I., Pun, I.-F. & Lien, C.-C. "Category-6" supertyphoon Haiyan in global warming hiatus: Contribution from subsurface ocean warming. *Geophys. Res. Lett.* **41**, 8547–8553 (2014).
15. Wada, A. & Usui, N. Importance of tropical cyclone heat potential for tropical cyclone intensity and intensification in the Western North Pacific. *J. Oceanogr.* **63**, 427–447 (2007).
16. Chu, J.-E. et al. Reduced tropical cyclone densities and ocean effects due to anthropogenic greenhouse warming. *Sci. Adv.* **6**, eabd5109 (2020).
17. Huang, P., Lin, I.-I., Chou, C. & Huang, R.-H. Change in ocean subsurface environment to suppress tropical cyclone intensification under global warming. *Nat. Commun.* **6**, 7188 (2015).
18. Patricola, C. M., Camargo, S. J., Klotzbach, P. J., Saravanan, R. & Chang, P. The influence of ENSO flavors on western North Pacific tropical cyclone activity. *J. Clim.* **31**, 5395–5416 (2018).
19. Yang, S. & Oh, J.-H. Effects of modes of climate variability on wave power during boreal summer in the western North Pacific. *Sci. Rep.* **10**, 5187 (2020).
20. Bister, M. & Emanuel, K. A. Low frequency variability of tropical cyclone potential intensity 1. Interannual to interdecadal variability. *J. Geophys. Res. Atmos.* **107**, ACL 26-21–ACL 26-15 (2002).
21. Emanuel, K. A. The dependence of hurricane intensity on climate. *Nature* **326**, 483–485 (1987).
22. Park, D.-S. R. et al. A performance evaluation of potential intensity over the tropical cyclone passage to South Korea simulated by CMIP5 and CMIP6 models. *Atmosphere* **12**, 1214 (2021).
23. Xu, J. & Wang, Y. Dependence of tropical cyclone intensification rate on sea surface temperature, storm Intensity, and size in the western North Pacific. *Wea. Forecast.* **33**, 523–537 (2018).
24. Wang, B. & Chan, J. C. L. How strong ENSO events affect tropical storm activity over the Western North Pacific. *J. Clim.* **15**, 1643–1658 (2002).
25. Zhao, H., Zhao, K., Klotzbach, P. J., Wu, L. & Wang, C. Interannual and interdecadal drivers of meridional migration of western North Pacific tropical cyclone lifetime maximum intensity location. *J. Clim.* **35**, 2709–2722 (2022).
26. Choi, Y., Ha, K.-J. & Jin, F.-F. Seasonality and El Nino diversity in the relationship between ENSO and western North Pacific tropical cyclone activity. *J. Clim.* **32**, 8021–8045 (2019).
27. Wu, M. C., Chang, W. L. & Leung, W. M. Impacts of El Niño-Southern Oscillation events on tropical cyclone landfalling activity in the western North Pacific. *J. Clim.* **17**, 1419–1428 (2004).
28. Fudeyasu, H., Iizuka, S. & Matsuura, T. Impact of ENSO on landfall characteristics of tropical cyclones over the western North Pacific during the summer monsoon season. *Geophys. Res. Lett.* **33**, L21815 (2006).
29. Zhang, W., Graf, H.-F., Leung, Y. & Herzog, M. Different El Niño types and tropical cyclone landfall in East Asia. *J. Clim.* **25**, 6510–6523 (2012).
30. Kim, H.-M., Webster, P. J. & Curry, J. A. Modulation of North Pacific tropical cyclone activity by three phases of ENSO. *J. Clim.* **24**, 1839–1849 (2011).
31. Yonekura, E. & Hall, T. M. ENSO Effect on East Asian Tropical Cyclone Landfall via Changes in Tracks and Genesis in a Statistical Model. *J. Appl. Meteor. Climatol.* **53**, 406–420 (2014).
32. Kim, H.-S., Kim, J.-H., Ho, C.-H. & Chu, P.-S. Pattern Classification of Typhoon Tracks Using the Fuzzy c-Means Clustering Method. *J. Clim.* **24**, 488–508 (2011).
33. Wang, S. & Toumi, R. On the intensity decay of tropical cyclones before landfall. *Sci. Rep.* **12**, 3288 (2022).
34. Park, D.-S. R., Ho, C.-H., Kim, J.-H. & Kim, H.-S. Strong landfall typhoons in Korea and Japan in a recent decade. *J. Geophys. Res. Atmos.* **116**, D07105 (2011).
35. Reynolds, R. W. et al. Daily high-resolution-blended analyses for sea surface temperature. *J. Clim.* **20**, 5473–5496 (2007).
36. Hersbach, H. et al. The ERA5 global reanalysis. *Q. J. R. Meteorol. Soc.* **146**, 1999–2049 (2020).
37. Slocum, C. J., Razin, M. N., Knaff, J. A. & Stow, J. P. Does ERA5 Mark a New Era for Resolving the Tropical Cyclone Environment? *J. Clim.* **35**, 7147–7164 (2022).
38. Kim, H.-M., Lee, M.-I., Webster, P. J., Kim, D. & Yoo, J. H. A physical basis for the probabilistic prediction of the accumulated tropical cyclone kinetic energy in the western North Pacific. *J. Clim.* **26**, 7981–7991 (2013).
39. Skamarock, W. C. et al. A description of the advanced research WRF model version 4. *National Center for. Atmos. Res.: Boulder, CO, USA* **145**, 145 (2019).
40. Zheng, Y., Alapaty, K., Herwehe, J. A., Del Genio, A. D. & Niyogi, D. Improving high-resolution weather forecasts using the Weather Research and Forecasting (WRF) Model with an updated Kain-Fritsch scheme. *Mon. Wea. Rev.* **144**, 833–860 (2016).
41. Kwon, Y. C. & Hong, S.-Y. A mass-flux cumulus parameterization scheme across gray-zone resolutions. *Mon. Wea. Rev.* **145**, 583–598 (2017).
42. Hong, S.-Y. & Lim, J.-O. J. The WRF single-moment 6-class microphysics scheme (WSM6). *Asia Pac. J. Atmos. Sci.* **42**, 129–151 (2006).
43. Lim, K.-S. S. & Hong, S.-Y. Development of an effective double-moment cloud microphysics scheme with prognostic cloud condensation nuclei (CCN) for weather and climate models. *Mon. Wea. Rev.* **138**, 1587–1612 (2010).
44. Hong, S.-Y., Noh, Y. & Dudhia, J. A new vertical diffusion package with an explicit treatment of entrainment processes. *Mon. Wea. Rev.* **134**, 2318–2341 (2006).
45. Noh, Y., Cheon, W., Hong, S. & Raasch, S. Improvement of the K-profile model for the planetary boundary layer based on large eddy simulation data. *Bound. -Layer. Meteorol.* **107**, 401–427 (2003).
46. Mlawer, E. J., Taubman, S. J., Brown, P. D., Iacono, M. J. & Clough, S. A. Radiative transfer for inhomogeneous atmospheres: RRTM, a validated correlated-k model for the longwave. *J. Geophys. Res. Atmos.* **102**, 16663–16682 (1997).
47. Dudhia, J. Numerical study of convection observed during the winter monsoon experiment using a mesoscale two-dimensional model. *J. Atmos. Sci.* **46**, 3077–3107 (1989).
48. Wang, S. & Toumi, R. Reduced Sensitivity of Tropical Cyclone Intensity and Size to Sea Surface Temperature in a Radiative-Convective Equilibrium Environment. *Adv. Atmos. Sci.* **35**, 981–993 (2018).

49. Chen, J. et al. Impacts of climate change on tropical cyclones and induced storm surges in the Pearl River Delta region using pseudo-global-warming method. *Sci. Rep.* **10**, 1965 (2020).

AUTHOR CONTRIBUTIONS

D.S.R.P. suggested the original idea and conceptualized the research. D.H.C. designed the model experiments. E.S. performed the calculations, and M.L. performed the model experiments. D.S.R.P. wrote the original draft of the manuscript and all the other authors contributed to revise the manuscript.

COMPETING INTERESTS

The authors declare no competing interests.

ADDITIONAL INFORMATION

Supplementary information The online version contains supplementary material available at https://doi.org/10.1038/s41612-023-00556-3.

Correspondence and requests for materials should be addressed to Doo-Sun R. Park or Dong-Hyun Cha.

Reprints and permission information is available at http://www.nature.com/reprints

Publisher's note Springer Nature remains neutral with regard to jurisdictional claims in published maps and institutional affiliations.